Numerical study of convection in the horizontal Bridgman configuration under the action of a constant magnetic field .2. Three-dimensional flow

H. Ben Hadid, Daniel Henry

J. Fluid Mech. (1997), *vol.* 333, *pp.* 57–83

Numerical study of convection in the horizontal Bridgman configuration under the action of a constant magnetic field. Part 2. Three-dimensional flow

By HAMDA BEN HADID AND DANIEL HENRY

Laboratoire de Mécanique des Fluides et d'Acoustique-UMR CNRS 5509, Ecole Centrale de Lyon/Université Claude Bernard-Lyon 1, ECL, BP 163, 69131 Ecully Cedex, France

(Received 6 December 1994 and in revised form 20 September 1996)

The effects of a constant magnetic field on electrically conducting liquid-metal flows in a parallelepiped cavity are investigated using a spectral numerical method involving direct numerical solution of the Navier–Stokes and Ohm equations for three-dimensional flows. Three horizontal Bridgman configurations are studied: buoyancy-driven convection in a confined cavity and in a cavity where the top boundary is a stress-free surface and thirdly, thermocapillary-driven flow in a cavity where the upper boundary is subjected to effects of surface tension. The results of varying the Hartmann number (Ha) are described for a cavity with $A_x = L/H = 4$ and $A_y = W/H = 1$, where L is the length, W is the width and H is the height of the cavity. In general, an increase in the strength of the applied magnetic field leads to several fundamental changes in the properties of thermal convection. The convective circulation progressively loses its intensity and when Ha reaches a certain critical value, which is found to depend on the direction (longitudinal or vertical) of the applied magnetic field, decrease of the flow intensity takes on an asymptotic form with important changes in the structure of the flow circulation. The flow structure may be separated into three regions: the core flow, Hartmann layers which develop in the immediate vicinity of the rigid horizontal boundaries or at the endwalls, and parallel layers appearing in the vicinity of the sidewalls. The behaviour of the maxima of velocity and of the overall flow circulation is found to depend on both the boundary conditions used and the direction of the applied magnetic field. Furthermore, the interaction of the electric current density with the applied magnetic field which leads to the structural reorganization described above can also create more subtle flow modifications, such as flow inversions which are observed mainly in the central region of the cavity.

1. Introduction

In this paper we focus on the behaviour of the flow of an electrically conducting liquid metal held in a differentially heated Bridgman boat and subjected to a constant magnetic field. In such a configuration convection flow in the melt is basically driven by two different sources: buoyancy and surface tension. Buoyancy convection arises from the imposed density gradients and gravity whereas thermocapillary-driven flows are the result of the presence of surface tension gradients at the free surface. Two

different aspects contributed to our interest in this problem: first, practical applications involving crystal growth depend on these types of convection; the second aspect is more theoretical and is that variety of different flow structures may occur in this very simple geometry, including the transition from steady laminar to turbulent flows.

In the absence of a magnetic field, it is well established from experimental (Hurle, Jakeman & Johnson 1974; Carruthers 1977; Kuhl & Wilke 1990) and theoretical (Gill 1974; Hart 1972, 1983; Laure & Roux 1987; Kuo & Korpela 1988; Wang *et al.* 1990) studies, that the convective circulation in a metallic liquid heated from the side exhibits a transition to oscillatory convection when the horizontal temperature gradient exceeds a certain critical value. These time-dependent flows give rise to fluctuations of the temperature field which, in turn, produce the oscillatory crystal growth responsible for the microscopically non-uniform distribution of dopant in the crystal. The origin of these time-dependent flows is not understood at present, but previous numerical calculations showed their existence even for zero Prandtl number, i.e. a situation in which the thermal field is fixed. This could indicate that the instabilities in such a type of flow have a dynamical nature. The magnetic field possesses many advantages, of which the principal one is its ability to penetrate solid walls and interact with the liquid metal held within. The use of a constant magnetic field in crystal growth can be justified by the tendency of the magnetic forces to inhibit the fluid velocity throughout the melt domain. Consequently, a magnetic field will tend to quench existing flow oscillations and thereby represents a promising method for improving crystal quality. While some of these features have been confirmed qualitatively in laboratory simulations (Müller 1993), quantitative results concerning the behaviour of the velocity, as well as the pattern of motion, can only be obtained through three-dimensional numerical simulations. Few numerical simulations have been performed in this field. A review of the progress and prospects of the use of a magnetic field in crystal growth can be found in a detailed paper by Series & Hurle (1991).

Experimental investigations by Hurle *et al.* (1974) in a differentially heated cavity of liquid gallium showed that the critical temperature difference for the appearance of flow oscillations decreases as the aspect ratios (A_x and A_y) of the cavity increase. Furthermore, it is seen that this critical temperature difference is sensitive to the presence of a transverse magnetic field and increases linearly with the square of the Hartmann number. Recent experiments by Pratte & Hart (1990) on liquid mercury ($Pr = 0.026$) carried out in a variety of closed rigid-wall containers with aspect ratios (length to width to height) of $4 \times 1 \times 1$, $4 \times 2 \times 1$ and $8 \times 8 \times 1$, and subjected to differential heating at the vertical endwalls, showed evidence of a stabilizing influence of the sidewalls. In fact, for the $4 \times 1 \times 1$ case, no time dependence was observed up to a Grashof number equal to 1.69×10^5, while for $4 \times 2 \times 1$ and $8 \times 8 \times 1$ the instabilities appear at 4.23×10^4 and 2.22×10^4 respectively. Their results also suggest that the dominant response near the onset of instability in the $4 \times 1 \times 1$ and $4 \times 2 \times 1$ cases consists of a standing wave. A similar stabilizing effect by the sidewalls on fluid convection has recently been analysed by Hung & Andereck (1988, 1990) who reported a series of measurements of thermal oscillations in mercury held in differentially heated boats with aspect ratios $4 \times 1 \times 1$ and $4 \times 2 \times 1$, and gave respectively 1.5×10^5 and 3.9×10^4 as values of the Grashof number for the emergence of a periodic state.

Three-dimensional numerical simulations of melt convection carried out by Baumgartl & Müller (1992) in a cylindrical geometry submitted to a constant magnetic field show that only the models including the electric potential equation agree well

with the experimental results. Experiments by Baumgartl, Hubert & Müller (1993) in a cylindrical container ($h/d = 1.9$, the height h is 64 mm and d is the diameter) filled with liquid gallium and submitted to a magnetic field $B_0 = 2\,\mathrm{mT}$ ($Ha = 5.8$) show temperature fluctuations when the temperature difference is equal to 0.65 K, corresponding to $Gr = 2.13 \times 10^6$ (the temperature difference for the transition from steady to unsteady flows is 0.6 K). Numerical simulations of the melt flow held in a geometry with similar characteristics ($Gr = 2.903 \times 10^6$ and $Ha = 5.8$) show time variation of the temperature fluctuations of a nearly sinusoidal form with typical amplitudes of about 4% of the mean values. For $Ha \geqslant 20$ ($B_0 \geqslant 7\,\mathrm{mT}$), flow fluctuations are suppressed and the resulting steady flow has essentially the same features as the unsteady one: a single roll slightly inclined with respect to the cylinder axis with small counter-rotating rolls, one near the top and one near the bottom. Furthermore, the numerical simulations show evidence that the induced magnetic field, generated by the liquid gallium flow across the field lines of the applied magnetic field, follows the oscillatory convection and the temperature variation. Ozoe & Okada (1989) investigated numerically three-dimensional buoyancy convection in a differentially heated cubical box with three different orientations of magnetic field along the axes. These authors have found that the magnetic field damps the flow most effectively when the magnetic field is imposed perpendicular to the heated vertical wall. It is the least effective when the magnetic field is horizontal and parallel to the heated vertical wall.

The onset of unsteady buoyancy-driven convection in a box has been analysed numerically by Afrid & Zebib (1990) for a melt with zero Prandtl number. Their results show that oscillations with a single frequency develop when Gr is 1.25×10^5 and 3×10^4 respectively for $4 \times 1 \times 1$ and $4 \times 2 \times 1$ confined cavities, while for cavities with a free surface, oscillations with a single frequency set in when Gr reaches 10^5 and 2.5×10^4 respectively for $4 \times 1 \times 1$ and $4 \times 2 \times 1$ geometries. Also their results show evidence of the stabilizing effects of rigid boundaries since the flow is more stable when the width of the cavity is reduced from 2 to 1 or when the top surface is rigid rather than free. In their computations Afrid & Zebib (1990) imposed a reflection symmetry about the longitudinal vertical centreplane to reduce the computation domain. This, however, restricts the possible solutions to symmetric ones. Our experience with oscillatory flows in three-dimensional cavities indicates that this symmetry is broken when periodic flows develop. Dupont *et al.* (1987) considered an open cavity with the aspect ratios $A_x = 4$ and $A_y = 2$ for $Pr = 0.069$. They found that for the steady state, the three-dimensional solution, which is a single stretched convection cell, differs greatly from the two-dimensional solutions and that the value of the critical Grashof number for the onset of unsteady flow is much larger than the one in the two-dimensional studies.

Steady three-dimensional combined buoyancy and thermocapillary-driven convection has been analysed by Mundrane & Zebib (1993). Their numerical computations were conducted in a cavity with aspect ratios $A_x = 1.47$, $A_y = 1.4$ and $Pr = 8.4$, and showed that at low Reynolds number, $Re = 349$, the three-dimensional solution agrees well with that obtained by a strictly two-dimensional model, whereas the solution at $Re = 23214$ shows the occurrence of a bifurcation from a steady two-dimensional to a steady three-dimensional flow. These authors, however, have not investigated the effect of a magnetic field.

Previous work on thermal convection under the action of a constant magnetic field has mainly been conducted for two-dimensional geometries (Ben Hadid, Henry & Kaddeche 1997; Oreper & Szekely 1983, 1984; Motakef 1990; Kim, Adornato & Brown 1988; Alboussière, Garandet & Moreau 1993; Kaddeche, Ben Hadid & Henry

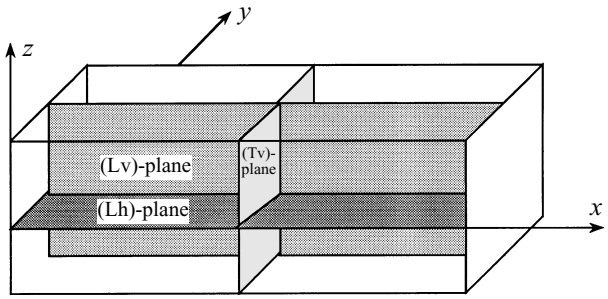

FIGURE 1. Model schematic of the parallelepipedic cavity. The left-hand and right-hand endwalls are cooled and heated, respectively. Location of the main planes: (Lv)-plane at $y = 0.5$; (Tv)-plane at $x = 2$ and (Lh)-plane at $z = 0$.

1994; Moreau & Ben Salah (1993, personal communication) and Bojarevics 1995). As for three-dimensional thermal convection, little is known about hydrodynamic aspects of the melt in the presence of a magnetic field.

In the present work a numerical approach is used to study the three-dimensional flow under the action of a constant magnetic field in a $4 \times 1 \times 1$ cavity with constant horizontal temperature gradient. The mathematical model constructed in §2 is based on the velocity–pressure equations with Ohm's law for the current density and the equation for charge conservation. The numerical model presented in §3 is based on the splitting method for time discretization and on the variational spectral method for space discretization. The effects of varying the Hartmann number, the orientation of the magnetic field and the dynamical boundary conditions for the three-dimensional model are discussed in §4. We consider two orientations of the magnetic field: the first one where the magnetic field is applied vertically in the positive z-direction is denoted the B_z case, and the second, where it is applied longitudinally in the positive x-direction is denoted the B_x case.

2. Mathematical model

We consider a parallelepiped cavity of aspect ratios $A_x = L/H = 4$ and $A_y = W/H = 1$ (where H is the height, W the width and L the length of the cavity, see figure 1) filled with electrically conducting liquid metal with a negligible electric charge density and submitted to a constant magnetic field. The top surface can be rigid, free or subject to a surface tension gradient. Owing to the temperature difference between the endwalls a horizontal temperature gradient forms throughout the cavity and generates laminar convective motion.

The basic equations used in the simulations of the melt flow are the Navier–Stokes equations including the Lorentz force, using the Boussinesq approximation for buoyancy since the metallic liquid is considered incompressible. The surface tension on the free surface is a linear function of temperature and is given by $\sigma = \sigma_0[1-\gamma(T-T_0)]$ where $\gamma = -(1/\sigma_0)(\partial\sigma/\partial T)$. The three-dimensional conservation equations of momentum are made dimensionless using H, H^2/ν, $U_{ref} = \nu/H$ and $\Delta T/A_x$ as scales for length, time, velocity and temperature respectively, where ν is the kinematic viscosity and $\Delta T = T_h - T_c$ is the difference of temperature between the vertical endwalls (T_h is imposed at the hot right endwall and T_c at the cold left endwall). Using these non-dimensionalizations, the governing equations in the melt

may be written as

$$\nabla \cdot \boldsymbol{v} = 0, \tag{2.1}$$

$$\frac{\partial \boldsymbol{v}}{\partial t} + (\boldsymbol{v} \cdot \nabla)\boldsymbol{v} = -\nabla p + \nabla^2 \boldsymbol{v} + Gr\theta \boldsymbol{e}_z + Ha^2 \boldsymbol{J} \times \boldsymbol{e}_B, \tag{2.2}$$

where $\boldsymbol{e}_B = \boldsymbol{B}/|\boldsymbol{B}|$, $\boldsymbol{v}$ is the dimensionless velocity field ($\boldsymbol{v} = (u, v, w)$), p denotes the dimensionless pressure and θ is the dimensionless temperature defined as $\theta = A_x(T - T_c)/\Delta T$. In the present study we set the Prandtl number equal to zero (highly thermally conducting fluid). Thus the temperature field is fixed, independent of fluid motion and has a linear variation given by $\theta = x$. The magnetic flux density vector $\boldsymbol{B}$ in the Lorentz force $\boldsymbol{J} \times \boldsymbol{B}$ is the sum of the flux densities of the applied magnetic field ($\boldsymbol{B}_0$) and the induced magnetic field $\boldsymbol{b}$ such that $\boldsymbol{B} = \boldsymbol{B}_0 + \boldsymbol{b}$. In general, for metallic liquid $\boldsymbol{b}$ is much smaller than $\boldsymbol{B}_0$, thus we assume that $\boldsymbol{b}$ is negligible and $\boldsymbol{B} = \boldsymbol{B}_0$. The electric current density, $\boldsymbol{J}$, which is normalized by $\sigma_e U_{ref} |\boldsymbol{B}_0|$, where σ_e is the electric conductivity of the melt, is given by Ohm's Law for a moving fluid:

$$\boldsymbol{J} = \boldsymbol{E} + \boldsymbol{v} \times \boldsymbol{e}_B \tag{2.3}$$

where $\boldsymbol{E}$ is the dimensionless electric field. Here, since all the melt flows studied are steady, the electric field can be written as the gradient of an electric potential ($\boldsymbol{E} = -\nabla\phi$). The equation of continuity for electric current density gives

$$\nabla \cdot \boldsymbol{J} = 0. \tag{2.4}$$

Equations (2.3) and (2.4) give

$$\nabla^2 \phi = \boldsymbol{e}_B \cdot (\nabla \times \boldsymbol{v}), \tag{2.5}$$

where ϕ is normalized by $H\, U_{ref} |\boldsymbol{B}_0|$. The boundary conditions associated with the above equations are at all rigid walls

$$u = v = w = 0, \tag{2.6}$$

and for the free surface case on $z = 1$ we have

$$w = \frac{\partial v}{\partial z} = \frac{\partial u}{\partial z} + Re \frac{\partial \theta}{\partial x} = 0. \tag{2.7}$$

Insulating conditions, $\boldsymbol{J} \cdot \boldsymbol{n} = 0$, are adopted for the electric current density $\boldsymbol{J}$ at all boundaries, where $\boldsymbol{n}$ denotes the normal to the boundary. With such a condition the value of the potential is not unique and needs thus to be fixed at one point of the cavity.

The dimensionless parameters appearing in equations (2.1)–(2.7), are the Grashof number $Gr = g\beta\Delta T H^4/L\nu^2$, the Reynolds–Marangoni number (called Reynolds number in the following) $Re = (-\partial\sigma/\partial T)\Delta T H^2/L\rho\nu^2$ and the Hartmann number $Ha = |\boldsymbol{B}_0| H(\sigma_e/\rho\nu)^{1/2}$, where β is the coefficient of volumetric expansion, g the gravity constant and ρ the fluid density.

3. Numerical procedure

3.1. *Time discretization*

Time discretization of the governing equations (2.1)–(2.5) is carried out using a high-order splitting algorithm for mixed stiffly stable schemes (Karniadakis, Israeli & Orszag 1991). From here on $\boldsymbol{N}(\boldsymbol{v}^n) = 0.5[\boldsymbol{v}^n \cdot \nabla \boldsymbol{v}^n + \nabla \cdot (\boldsymbol{v}^n \boldsymbol{v}^n)]$ represents the nonlinear

contribution written in skew-symmetric form for aliasing control. First, considering the nonlinear term, we obtain for the velocity

$$\boldsymbol{v}^{n+1/3} - \sum_{q=0}^{J-1} \alpha_q \boldsymbol{v}^{n-q} = \Delta t \left\{ \sum_{q=0}^{J-1} \beta_q [-\boldsymbol{N}(\mathbf{v}^{n-q})] + Gr\theta \boldsymbol{e}_z + Ha^2 \boldsymbol{J} \times \boldsymbol{e}_B \right\}, \tag{3.1}$$

where α_q, β_q are implicit/explicit weight coefficients for stiffly stable schemes of order J ($J = 2$). The next substep incorporates the pressure equation and enforces the incompressibility constraint:

$$\boldsymbol{v}^{n+2/3} - \boldsymbol{v}^{n+1/3} = -\Delta t \nabla p^{n+1}, \tag{3.2}$$

$$\nabla \cdot \boldsymbol{v}^{n+2/3} = 0. \tag{3.3}$$

Finally, the last substep includes the viscous correction and the imposition of the boundary conditions, i.e.

$$\gamma_0 \boldsymbol{v}^{n+1} - \boldsymbol{v}^{n+2/3} = \Delta t \nabla^2 \boldsymbol{v}^{n+1}, \tag{3.4}$$

where γ_0 is a weight coefficient of the backwards differentiation scheme employed (Karniadakis *et al.* 1991). This fractional scheme is implemented by solving the pressure equation in the form

$$\nabla^2 p^{n+1} = \nabla \cdot \left(\frac{\boldsymbol{v}^{n+1/3}}{\Delta t} \right). \tag{3.5}$$

The consistent high-order pressure boundary condition associated with the pressure equation is derived from the equations of motion in which the linear term is written as $\nabla^2 \boldsymbol{v} = \nabla(\nabla \cdot \boldsymbol{v}) - \nabla \times \nabla \times \boldsymbol{v}$. This gives

$$\frac{\partial p}{\partial \boldsymbol{n}} = \boldsymbol{n} \cdot \left(-\sum_{q=0}^{J-1} \beta_q [\boldsymbol{N}(\boldsymbol{v}^{n-q}) + \nabla \times (\nabla \times \boldsymbol{v}^{n-q})] + Gr\theta \boldsymbol{e}_z + Ha^2 \boldsymbol{J} \times \boldsymbol{e}_B \right), \tag{3.6}$$

where $\boldsymbol{n}$ denotes the normal to the boundary Γ.

3.2. *Spatial discretization and accuracy*

The spatial discretization of the above system of equations is obtained using a spectral-element methodology (Patera 1984). More specifically, in the standard spectral-element discretization, the unknowns and data are expressed as tensorial products using Lagrange polynomial interpolants. The final system of discrete equations is then obtained via a Galerkin variational method. The code used here has been extensively tested in the case of steady and unsteady natural convection in two-dimensional rectangular cavities and the results have been compared with published data (Ben Hadid & Roux 1990*a*, *b*, 1992; Roux 1990). Further extensive verifications for the convective flow in a three-dimensional confined cavity with aspect ratios $2 \times 1 \times 1$ (respectively for the x-, y- and z-directions) and $Pr = 0$ have been performed by comparisons with a second numerical code (Carrière & Jeandel 1991) based on a finite-element method which used a highly refined mesh ($67 \times 33 \times 33$). The two codes produce quantitatively comparable results and give similar behaviours when the Grashof number is increased up to $Gr = 2.5 \times 10^5$. In addition the transition from steady to unsteady flows is obtained in the same range of Grashof number with a good agreement for the characteristics of the unsteady flows.

The cavity is discretized using the Chebyshev–Gauss–Lobatto points distribution

	$27 \times 15 \times 15$			$31 \times 15 \times 17$			$33 \times 15 \times 19$		
Re	u_{max}	v_{max}	w_{max}	u_{max}	v_{max}	w_{max}	u_{max}	v_{max}	w_{max}
3×10^3	393.90	86.783	230.07	393.41	92.241	224.71	393.64	96.927	226.62
5×10^3	568.77	141.001	334.93	570.06	128.41	342.25	569.34	128.38	340.52

TABLE 1. Tests of numerical accuracy for the thermocapillary case

Grid	u_{max}	v_{max}	w_{max}
$27 \times 15 \times 15$	2.802×10^{-2}	5.768×10^{-3}	2.730×10^{-2}
$35 \times 17 \times 17$	2.833×10^{-2}	6.012×10^{-3}	2.722×10^{-2}
$39 \times 17 \times 19$	2.820×10^{-2}	5.848×10^{-3}	2.754×10^{-2}

TABLE 2. Tests of numerical accuracy for the confined cavity with magnetic field ($Gr = 10^4$ and $Ha = 100$)

with typically $27 \times 15 \times 15$ (respectively for the x-, y- and z-directions) mesh points for the confined cavity. For the thermocapillary case most of the simulations have been done with $31 \times 15 \times 17$ mesh points. To ensure that the solutions are accurate and that the phenomena are not spurious artifacts of poorly resolved grids, grid sensitivity studies have been conducted for the thermocapillary case for two values of the Reynolds number, $Re = 3 \times 10^3$ and 5×10^3, for which the flow is found to be steady. The results can be found in table 1 which gives the maxima of the velocity obtained on the collocation points for three different meshes.

When the grid is refined from $27 \times 15 \times 15$ to $31 \times 15 \times 17$ the maxima of the main velocity components agree within 2.14% for the higher of the investigated Reynolds numbers, $Re = 5 \times 10^3$, and within 2.4% for $Re = 3 \times 10^3$. The results also show clearly that for $Re = 5 \times 10^3$ an increase of the number of grid points from $31 \times 15 \times 17$ to $33 \times 15 \times 19$ leads to 0.51% and 0.22% variations, respectively, for the maxima of the vertical and horizontal component of the velocity. These variations are 0.84% and 0.06% for $Re = 3 \times 10^3$. However for v, which is the smallest velocity component in the flow, when changing the grid from $31 \times 15 \times 17$ to $33 \times 15 \times 19$ the variation is about 5% for $Re = 3 \times 10^3$, but it is only 0.023% for $Re = 5 \times 10^3$. Note that the value of the maximum of the velocity is generally underestimated if it is not on the collocation points, so that a small change in the number of grid points may then produce a relatively large variation on this value. This explains the small discrepancies observed for the v-component of the velocity. Therefore, the $31 \times 15 \times 17$ grid is considered sufficiently fine to resolve the flow adequately for the thermocapillary flow.

The effect of the grid has also been investigated for the case with a magnetic field by comparing the results obtained for the confined cavity ($Gr = 10^4$ and $Ha = 100$) and different grids. The details of the grid influence on the maximum values of the velocities are given in table 2. This table shows that the maximum variations of u_{max}, v_{max} and w_{max} with respect to the grid change are less than 1.1%, 4.5% and 1.2% respectively. Thus, a satisfactory accuracy can be reached with the lowest grid (i.e. with $27 \times 15 \times 15$ points) in the case of the confined cavity with a magnetic field.

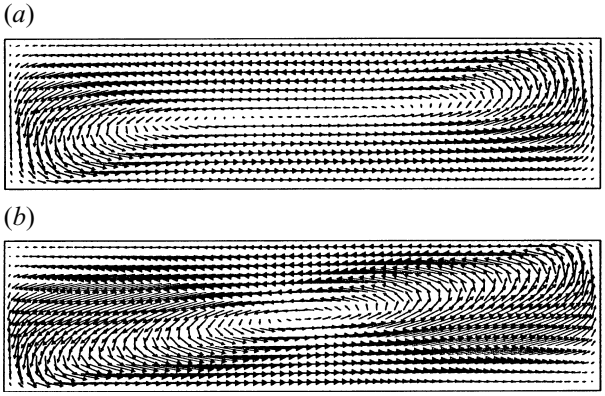

FIGURE 2. Steady flow solutions represented by a single rotating cell, in a confined cavity without magnetic field ($Ha = 0$). Velocity vectors projected on the (Lv)-plane for two Grashof numbers: (*a*) $Gr = 10^4$ and (*b*) $Gr = 4 \times 10^4$.

4. Numerical results

This paper focuses on the changes in the characteristics of the liquid-metal flow as the Hartmann number is increased. We also want to illustrate the sensitivity of the results to changes in the upper dynamical boundary condition by considering three cases for which the upper boundary is a rigid wall, stress free or subject to a surface tension gradient. The Hartmann number varies from zero to 200 and only the results for two magnetic field orientations, namely, the x- and z-directions, will be discussed here. In the present study we set the Grashof number equal to 10^4 for the buoyancy-driven flow and the Reynolds number equal to 2×10^3 for the thermocapillary-driven flow. These values being much lower than the critical values for the onset of the oscillatory flow, the expected flows will be steady.

The symmetries of the original buoyancy-induced flow in differentially heated parallelepiped cavities in the confined case are a reflection symmetry with respect to the (Lv)-plane (longitudinal vertical centreplane) and a reflection symmetry with respect to the (Th)-line (transverse horizontal centreline, at the intersection of the (Tv)-plane (transverse vertical centreplane) and of the (Lh)-plane (longitudinal horizontal centreplane)). The combination of these two symmetries gives a further symmetry with respect to the centrepoint of the cavity. These different centreplanes which will be used for graphical representation of the results are shown in figure 1. If we consider a free surface, with or without surface tension effects, the upper and lower boundary conditions are different, and only the symmetry with respect to the (Lv)-plane holds. These symmetries are usually broken as the flow becomes unsteady with increasing Gr (for example through a Hopf bifurcation). Here, since we study steady flows which will be reduced in intensity by the application of a magnetic field, no such symmetry breaking is expected and the original symmetries will be maintained

4.1. *Confined cavity*

The three-dimensional steady flows in a parallelepiped confined cavity are illustrated by means of plots of the velocity vectors in the (Lv)-plane for two Grashof numbers ($Gr = 10^4$ and 4×10^4). In figure 2 we can see that the three-dimensional flow differs noticeably from its two-dimensional counterpart. In the range of Grashof numbers considered, $Gr \leqslant 4 \times 10^4$, the three-dimensional calculations exhibit a single large convective circulation in the plane of symmetry (Lv-plane), whereas in the two-

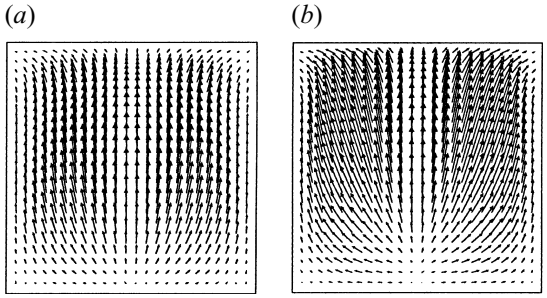

FIGURE 3. Steady flow solutions in a confined cavity without magnetic field ($Ha = 0$). Velocity vectors projected on a plane located at $x = 3.75$ for two Grashof numbers: (*a*) $Gr = 10^4$ and (*b*) $Gr = 4 \times 10^4$.

dimensional model, a steady bifurcation leads to the appearance of a multi-cellular flow for Gr around 2×10^4, and is followed by the onset of oscillations at Gr about 2.5×10^4 (Roux 1990). Note that even at a moderate value of the Grashof number ($Gr = 10^4$), the calculated solution captures three-dimensional flow structures with transverse variations in velocity profiles. The three-dimensional character of the flow is particularly strong near the endwalls, as shown in figure 3.

In order to characterize the effects of a constant magnetic field applied vertically (the B_z case) in a three-dimensional geometry, we plot in figure 4 the velocity vectors in the (Tv)- and (Lh)-planes for $Gr = 10^4$ and $Ha = 100$. A strong magnetic field has two important effects: a large reduction of the magnitude of the velocity and a dramatic modification of the structure of the flow. From the results it appears that when Ha is increased from zero to $Ha = 10$, the shape of the initial velocity profiles due to pure buoyancy convection (i.e. $Ha = 0$) changes slightly. When $Ha > 10$, two symmetrical maxima of velocity become apparent. When the value of Ha increases further, these maxima become peaks which are the dominant features of the velocity profiles, and are shifted towards the vertical sidewalls (figure 4). At the same time, in the vicinity of these walls, the velocity gradients become larger and give rise to boundary layers. These results in the (Tv)-plane compare well with the fully established bidimensional results calculated in such transverse planes (R. Moreau & N. Ben Salah 1993, personal communication; Bojarevics 1995). From figure 4 it is clear that the magnetic field induces important changes in the horizontal velocity profiles as well as in the vertical velocity profiles. However, in the vertical velocity profiles the peaks are less pronounced. This effect may be due to the fact that in the regions near the endwalls there is no direct damping of the flow since the velocity is parallel to the magnetic field lines. Inspection of figure 4 also reveals that the structure of the flow remains symmetrical with respect to the (Lv)-plane. As Ha is increased, the flow becomes progressively more independent of x in the central part of the cavity and antisymmetric with respect to the (Lh)- and (Tv)-planes. Note that, in the core region, the horizontal velocity profile displays a linear variation with respect to the vertical coordinate (z-shaped profile). Furthermore, for large Hartmann number ($Ha = 100$), examination of the flow structure in the (Lv)-plane reveals the existence of two secondary recirculation zones inside the global circulation in the vicinity of the endwalls. These last two features have been already observed in two-dimensional simulations (Ben Hadid *et al.* 1997).

It must be noted that the general behaviour of the convective flow development was not found in the two-dimensional simulation and is a reflection of a specifically three-

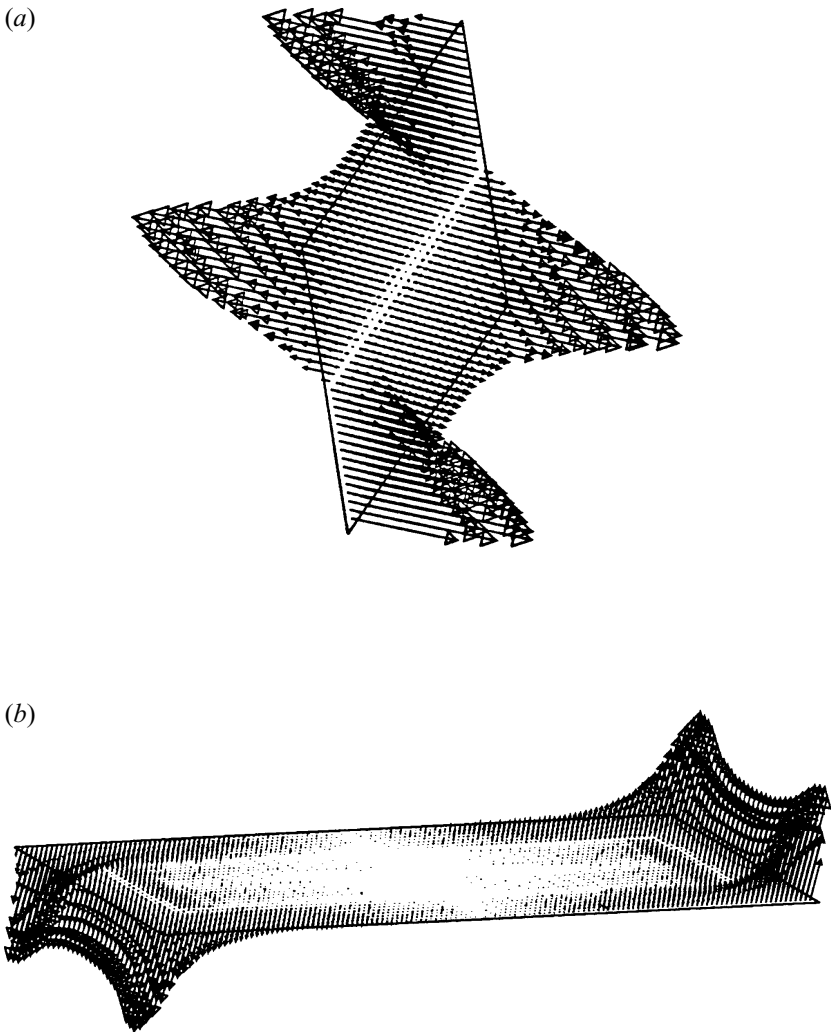

FIGURE 4. Flow solutions in the confined cavity for the B_z case for $Gr = 10^4$ and $Ha = 100$. Velocity vectors in the (Tv)-plane (*a*) and in the (Lh)-plane (*b*).

dimensional mechanism of interaction between the magnetic field and the electric current induced in the melt moving in a magnetic field. Some insight into the effects of the electric current can be obtained in a qualitative manner from the plots of the electric potential ϕ and the electric current density vector $\boldsymbol{J}$ displayed respectively in figures 5 and 6. The overall mechanism generating the electric current in such configurations may be viewed as follows. Since $\boldsymbol{B}$ is vertical, the directly induced electric current ($\boldsymbol{v} \times \boldsymbol{B}$) due to the motion of the fluid in any plane of constant x is horizontal, going in opposite directions in the lower and upper parts. As the walls are electrically insulating, conservation of current makes the current lines closed, and hence vertical currents appear along the vertical sidewalls. These currents are created by vertical gradients of electric potential, but this potential also creates horizontal currents near the corners which compete with the directly induced current. The resulting total current forms loops in the sense dictated by ($\boldsymbol{v} \times \boldsymbol{B}$), away from the corners. There is a counter-rotating current circulation in the corners due to the

electric potential current which is dominant near the upper and lower walls where ($\boldsymbol{v} \times \boldsymbol{B}$) is zero (rigid wall) (see figure 6). The resulting current is responsible for the creation of electromagnetic forces which strongly decelerate the motion, except in the parallel layers along the lateral walls where the current is nearly parallel to the applied magnetic field. The appearance of overvelocities in these layers is thus a direct consequence of the structure of the electric current. Furthermore, from figure 6 it is clear that in the central region the electric potential is nearly uniform, i.e. that E is small, and the dominant contribution to the electric current $\boldsymbol{J}$ is then from the direct term $\boldsymbol{v} \times \boldsymbol{B}$, which corresponds to the electric model used in two-dimensional situations. This explains why, in such regions, behaviour similar to that of the two-dimensional case is found.

Additional information may be obtained from figure 7 where the maxima of the absolute values of the horizontal and vertical velocities, denoted respectively by u_{max} and w_{max}, are plotted. In this figure the maxima of these two components in the (Lv)-plane, denoted by u_{mil} and w_{mil} respectively, are also given. These curves reveal the change in the dynamics of the flow as the Hartmann number is increased, and, for $Ha \geqslant 10$, the maxima are found to vary as

$$u_{max} \sim Ha^{-1} \tag{4.1a}$$

and

$$w_{max} \sim Ha^{-1}, \tag{4.1b}$$

whereas the dependence in the (Lv)-plane is close to that of the two-dimensional simulations (Ben Hadid *et al.* 1997) with

$$u_{mil} \sim Ha^{-2} \tag{4.2a}$$

and

$$w_{mil} \sim Ha^{-3/2}. \tag{4.2b}$$

The possible explanation of the dependence of u_{max} and w_{max} on Ha^{-1} may be obtained from the following analysis: in the core region the only contribution to the electric current, J_c, is from $\boldsymbol{v} \times \boldsymbol{B}$ and since $u_c \sim Ha^{-2}$ thus $J_c \sim Ha^{-2}$. In the core region the electric current in a transverse section circulates horizontally over a layer of thickness $1/2$ while it circulates vertically along the lateral walls over the parallel layer of thickness $\delta_{\|} \sim Ha^{-1/2}$. Using the conservation of the electric current we obtain for the electric current in the parallel layer $J_p \sim Ha^{-3/2}$. Moreover, the only contribution to the electric current, J_p, is from the vertical electric potential gradient, therefore $J_p \sim \Delta\phi/\Delta z$, and since the relevant vertical length scale for the potential is 1, the maximum difference in the electric potential is $\Delta\phi \sim Ha^{-3/2}$. Finally, in the parallel layer the horizontal electric potential gradient (i.e. $\Delta\phi/\delta_{\|} \sim Ha^{-1}$) is balanced by $\boldsymbol{v} \times \boldsymbol{B}$ which gives a Ha^{-1} variation for u in the parallel layer where the velocity reaches its maximum value. The conservation of the flow rate between the longitudinal circulation and the vertical circulation along the endwalls gives the same Ha^{-1} variation for w_{max}because both circulations occur in parallel layers of thickness $Ha^{-1/2}$.

We next examine the interaction between the flow and the magnetic field when it is applied horizontally, in the x-direction. In figure 8, where the velocity vectors in the (Tv)- and (Lh)-planes are plotted, it is clear that the horizontal magnetic field induces changes in the structure of the flow as its strength is increased. It appears that the progressive structural changes in the horizontal velocity are, in a qualitative sense,

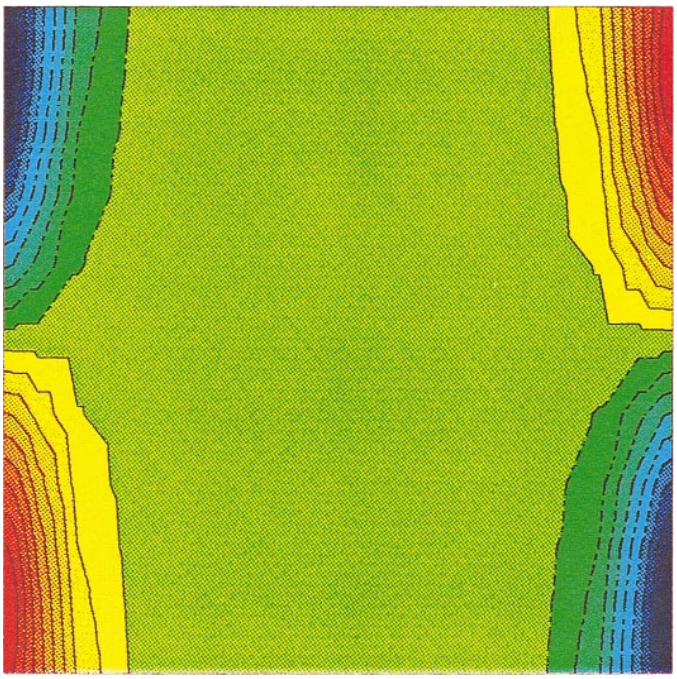

FIGURE 5. The electric potential field in the (Tv)-plane (viewed from the right) for the confined cavity and the B_z case. $Gr = 10^4$ and $Ha = 200$.

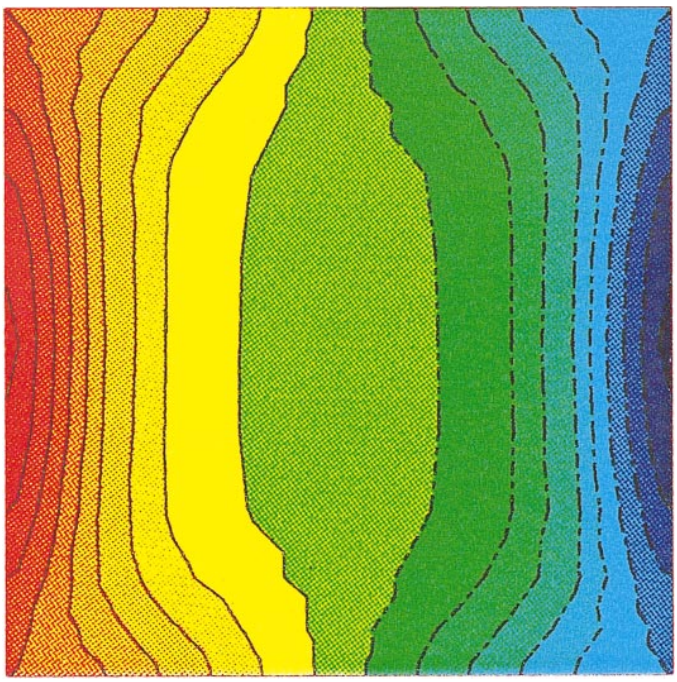

FIGURE 10. The electric potential field in a plane located at $x = 0.5$ (viewed from the right) for the confined cavity and the B_x case. $Gr = 10^4$ and $Ha = 200$.

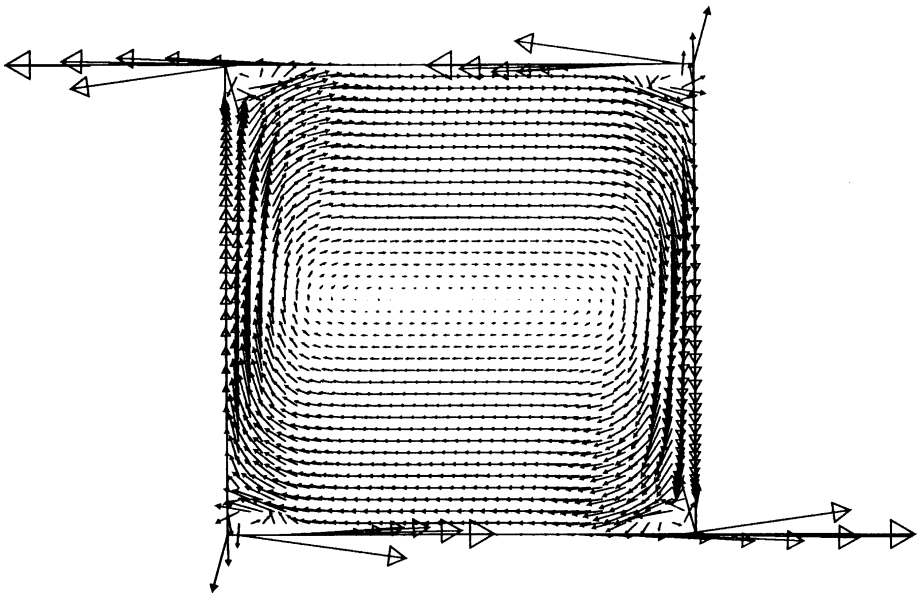

FIGURE 6. The electric current density vectors projected on the (Tv)-plane (viewed from the right) for the confined cavity and the B_z case. $Gr = 10^4$ and $Ha = 200$.

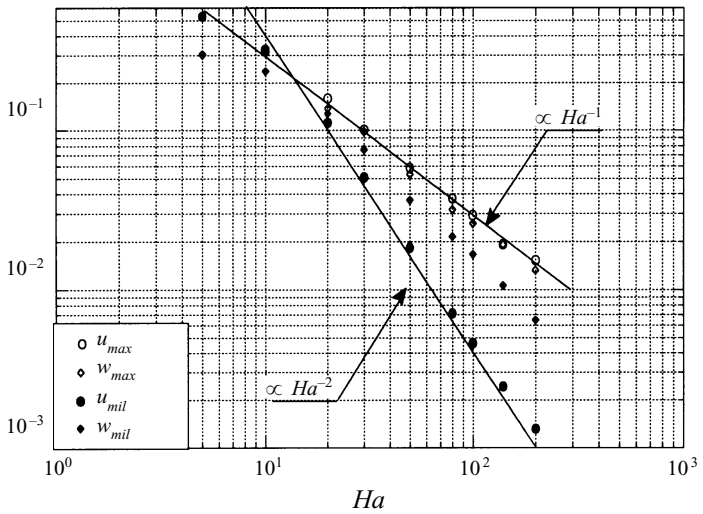

FIGURE 7. Plots of the maxima of the two main components of the velocity for the confined cavity and the B_z case for various Hartmann numbers. u_{max} and w_{max} correspond to the maxima in the whole cavity, u_{mil} and w_{mil} correspond to the maxima in the (Lv)-plane.

similar to those observed in the B_z case, but the value of Ha at which they become significant is larger. Low values ($Ha \leqslant 50$) have little influence on the configuration of the horizontal velocity, whereas when it becomes large enough ($Ha = 200$) we observe two maxima near the lateral walls in the lower and upper parts of the profiles. However, the size of these peaks corresponds to that obtained for much lower values of Ha in the B_z case. Furthermore, examination of the velocity vectors in the (Lh)-plane shows evidence of important modification in the profile of the vertical

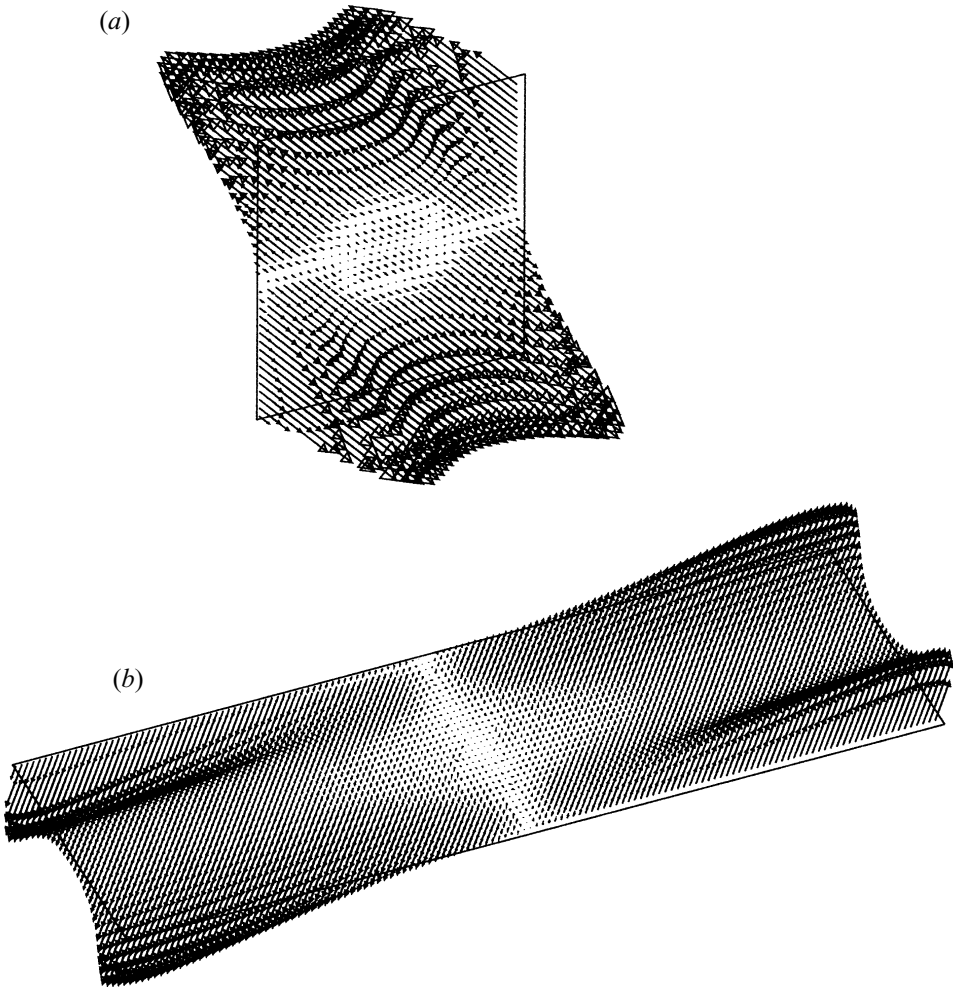

FIGURE 8. Flow solutions in the confined cavity for the B_x case for $Gr = 10^4$ and $Ha = 200$. Velocity vectors in the (Tv)-plane (*a*) and in the (Lh)-plane (*b*).

velocity and reveals that the vertical velocity decreases faster in the core region. Thus, two layers which are symmetrical with respect to the (Lv)-plane are created parallel to the vertical lateral walls and, unlike the B_z case, the upward and downward vertical velocities in the parallel layers extend into the central region of the cavity. In fact, in the B_x case, the main effects relate to the vertical velocity, which is perpendicular to $\boldsymbol{B}$, whereas in the B_z case it was the horizontal velocity which showed the important changes.

When $\boldsymbol{B}$ is in the x-direction, the directly induced electric current comes principally from interaction with the vertical velocity component, mainly near the side- and endwalls. This current is transverse, in the direction of positive y in the right-hand side of the cavity, and in the opposite direction in the left-hand side. The conservation of the current still occurs mainly in planes of constant x, with the creation of two superposed counter-rotating loops (see figure 9*a*), with opposite senses of rotation in the right- and left-hand parts of the cavity. The electric potential responsible for this is plotted in figure 10 (see page 68): the potential is antisymmetric with

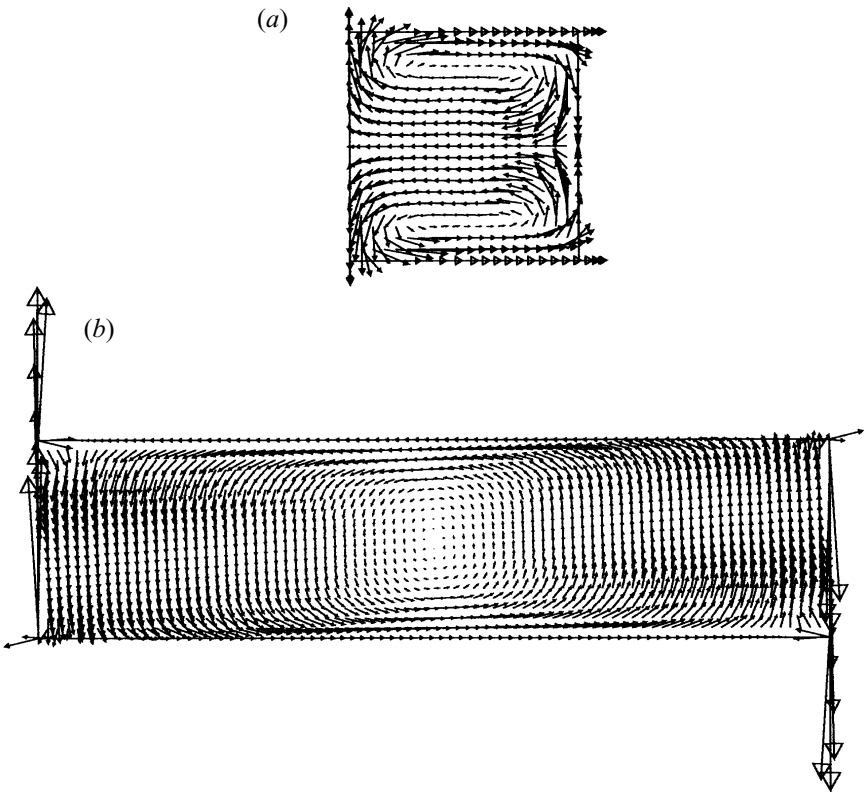

FIGURE 9. The electric current density vectors projected on a plane located at $x = 0.5$ (viewed from the right) (*a*) and on the (Lh)-plane (*b*), for the confined cavity and the B_x case. $Gr = 10^4$ and $Ha = 200$.

respect to the (Lv)-plane and gives gradients in planes of constant x tending to create recirculation zones of current; it is also of opposite signs in the right- and left-hand parts of the cavity (antisymmetry with respect to the Th-axis), which generates smaller longitudinal gradients responsible for a longitudinal current circulation (its maximum is two-times smaller than the transverse current recirculation) which is clearly visible in the (Lh)-plane (figure 9*b*). The electric potential in planes of constant z is in fact roughly similar to that obtained in planes of constant x in the B_z case.

An understanding of the action of the magnetic field upon the melt flow through the electric current density is necessary to explain the unexpected flow structure modifications such as the reverse flow observed in the core region in a small area around the centre of the (Tv)-plane (see figure 8*a*). It is clear that the currents act directly through the Lorentz force ($\boldsymbol{J} \times \boldsymbol{B}$) to reduce the vertical velocity component around mid-height in the cavity (except near the lateral walls where the current is no longer horizontal and where relatively large velocities are obtained). In contrast, the origin of the structural change mentioned above, and its relationship with the electromagnetic forces, may be found from the analysis of the pressure field changes induced by the electric current. The electric current loops observed in planes of constant x, perpendicular to the applied magnetic field, generate concentric electromagnetic forces, which are either convergent or divergent depending on the sense of circulation, and give rise to local overpressures and underpressures respectively. For example in the plane $x = 0.5$ (figure 9*a*), the upper loop generates convergent forces and a

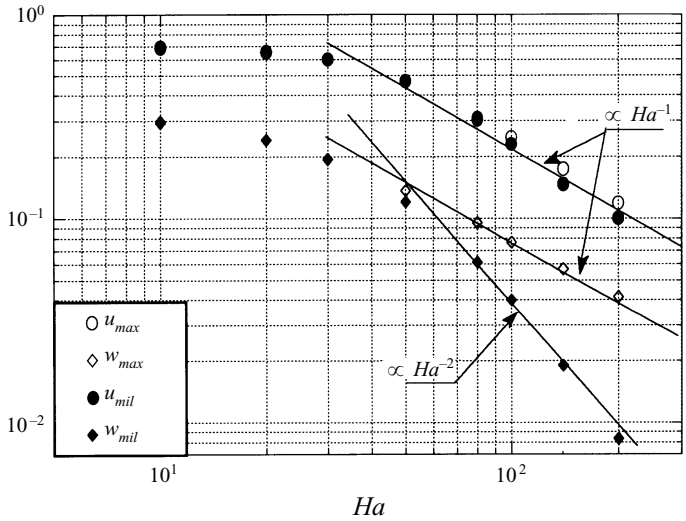

FIGURE 11. Plots of the maxima of the two main components of the velocity for the confined cavity and the B_x case for various Hartmann numbers. u_{max} and w_{max} correspond to the maxima in the whole cavity, u_{mil} and w_{mil} correspond to the maxima in the (Lv)-plane.

local overpressure, whereas the lower loop generates divergent forces and therefore a local pressure decrease. Thus, in addition to the pressure gradient of pure buoyancy convection (producing the longitudinal circulation of the flow), the electric current circulation induces new longitudinal pressure gradients which may be responsible for the appearance of the observed reverse flow.

As a starting point for further discussion of the flow behaviour, the maxima of the velocity over the whole cavity and in the (Lv)-plane are plotted in figure 11. The effect of the reduction of flow intensity with increasing Hartmann number is small for $Ha \leqslant 20$, but becomes remarkably important when the Hartmann number is large. It is clear from the figure that relations (4.1*a*), (4.1*b*) also holds for large Hartmann numbers, that is $Ha \geqslant 50$. In contrast to the B_z case, it is now w_{mil} which decreases in proportion to Ha^{-2}, whereas u_{mil} decreases roughly as Ha^{-1}. It is not surprising that the asymptotic character is reached at higher values of Ha compared to the B_z case since the relevant length scale is the distance between the Hartmann walls which is increased by a factor of four.

4.2. *Cavity with a free surface (Re = 0)*

In the absence of a magnetic field a steady-state solution is obtained for $Gr = 10^4$. In such a configuration, the flow pattern consists of a long circulation cell filling the whole cavity, and the maximum of the velocity is reached at the surface in the region of the cold wall. The flow has a three-dimensional character and transverse velocities are present, particularly near the endwalls. Furthermore, examination of the transverse surface velocity profile reveals that its shape evolves progressively along x from a U-shape near the hot wall to a Poiseuille-like shape. Note that this unicellular flow circulation is found for all the Grashof numbers studied, $Gr < 4 \times 10^4$, for which the flow was found to be steady. In contrast, in the two-dimensional studies the convection cell splits into two cells which begin to oscillate with a single frequency at Gr about 13 750. This critical Grashof number rises slightly to 14 750 when the Prandtl number is increased from zero to 0.015 (Ben Hadid & Roux 1992).

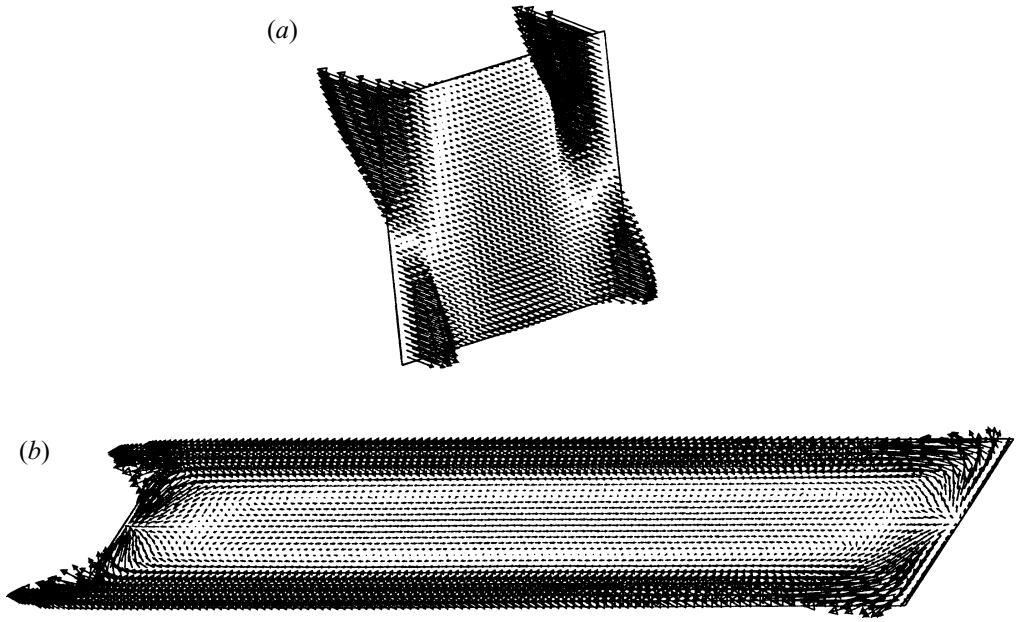

FIGURE 12. Flow solutions for the free-surface cavity and the B_z case for $Gr = 10^4$ and $Ha = 140$. Velocity vectors in the (Tv)-plane (*a*) and at the free surface (*b*).

Upon the imposition of the vertical magnetic field, the absolute values of the velocity are reduced and the circulation tends to separate into two symmetrical lateral layers. The departure from the initial flow structure appears, as in the confined cavity case, for $Ha \geqslant 10$, which suggests that at this value of Ha the damping force contributes significantly to the modification of the melt flow. It is interesting to observe in figure 12(*a*) that the maxima of the velocity are located near the free surface and that they have shifted progressively toward the sidewalls as Ha is increased. This transverse variation is also visible over the whole (Tv)-plane, and the most vigorous flow activity in the x-direction is in fact limited to a small region in the immediate vicinity of the lateral walls which is the parallel layer. In figure 12(*a*), the plots of the velocity vectors given for $Ha = 140$ show all the characteristics of the large-Ha solution and reveal how the flow in the parallel layers matches the core flow. A consequence of the strong damping effect of the magnetic field is the appearance of a reverse flow in the upper part of the core over a small region which increases in size as Ha increases; at $Ha = 140$, it roughly covers the core region. The surface velocity vectors displayed in figure 12(*b*) for $Ha = 140$ give an example of the structure of the flow at the surface. From the figure it is clear that the reverse flow which extends over almost the whole length of the cavity appears to constrain the upstream flow to go towards the lateral walls and thence to feed the parallel layers. The modification of the flow structure in the (Lh)-plane looks similar to that obtained in the confined cavity case.

The equipotential lines and electric current density vectors, which give further insight into the damping effects of the magnetic forces, have globally a similar structure to those obtained in the confined cavity case. The electric potential field is antisymmetric with respect to the (Lv)-plane, but, in contrast with the confined cavity case, it does not take on the antisymmetry with respect to the (Lh)-plane as Ha is increased. Furthermore, unlike the confined cavity case, the electric potential in the central region is not uniform. The equipotential lines are nearly straight, parallel to

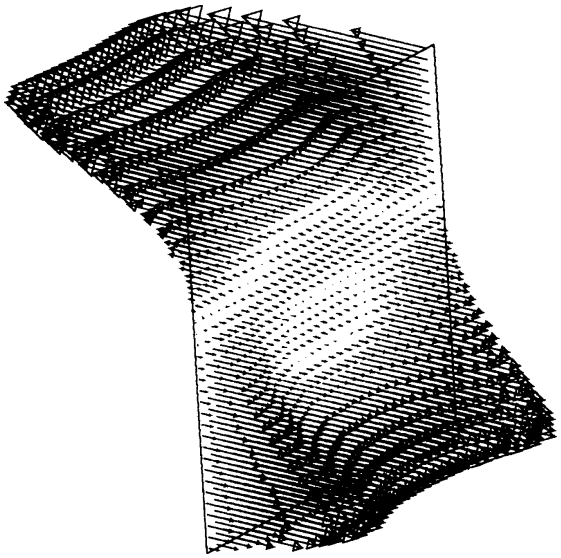

FIGURE 13. Flow solutions for the free-surface cavity and the B_x case. Velocity vectors in the (Tv)-plane for $Gr = 10^4$ and $Ha = 200$.

the imposed magnetic field, which results in a new contribution to the magnetic force, enhancing the damping effect in the upper part and decreasing it in the lower part. In the centre of the upper part, this effect produces an electromagnetic force which ultimately, as *Ha* increases, overcomes the driving pressure force and induces a reverse flow. An important fact is that in the centre part, while the directly induced electric current depends on the local velocity, in contrast, the potential current due to $\boldsymbol{E}$ could be connected to the strong potential created in the parallel layers and so to the vorticity in these zones. Since this vorticity decreases less than the velocity in the core region as *Ha* is increased, $\boldsymbol{E}$ can give currents tending to reverse the flow in this core region. Finally, owing to the free-surface dynamical boundary condition, the electric current density field does not display at the upper corners the small counter-rotating loops of current which were observed in the confined cavity case.

We next examine the effect of the magnetic field when it is applied horizontally in the positive x-direction. Modifications in the flow structure arise from increasing the intensity of the magnetic field. The evolution of the structure of the vertical velocity is qualitatively similar to that observed in the confined cavity for the B_x case. However, from figure 13 we can see that the behaviour of the horizontal velocity is somewhat different from that observed in a confined cavity. In fact, the overvelocities are small and only apparent in the lower part of the cavity, whereas in the layer near the top surface the velocity has a nearly uniform profile in the y-direction.

The structures of the electric potential field and of the electric current density vector field, which are responsible for the modifications of the flow behaviour when *Ha* is increased, are roughly similar to those obtained for the confined cavity, except that no symmetry holds with respect to the (Lh)-plane because of the presence of the free surface. As already observed in the confined cavity case, two superposed counter-rotating loops are found in planes of constant x, which generate pressure effects and hence small longitudinal reverse flows which are clearly visible in the plot of the velocity vectors shown in figure 13.

In an attempt to give quantitative results indicating the action of the magnetic field,

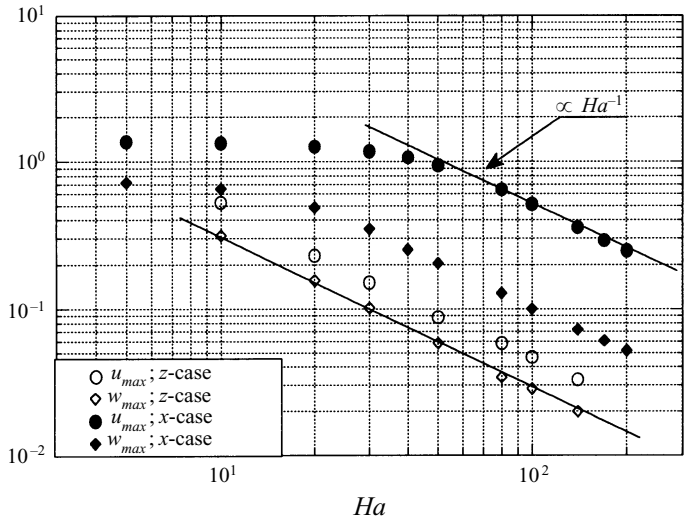

FIGURE 14. Plots of the maxima of the two main components of the velocity (u_{max} and w_{max}), for the free-surface cavity case. The data are plotted as a function of the Hartmann number for the B_z and the B_x cases.

we plot the maxima of the velocity in figure 14. Examination of this figure shows qualitative behaviour similar to that observed in the confined cavity and reveals that both the maxima of the velocities now behave as Ha^{-1} above about $Ha = 10$ in the B_z case, while in the B_x case this occurs at about $Ha = 50$ for u_{max} and earlier at about $Ha = 20$ for w_{max}.

4.3. *Thermocapillary-driven flow ($Re \neq 0$, $Gr = 0$)*

Three-dimensional calculations performed up to $Re = 5 \times 10^3$ show steady-state solutions which, as previously found in two-dimensional calculations (Ben Hadid & Roux 1992), present a concentrated circulation located in the region near the cold wall. The flow structure for three Re values is presented in figure 15 as a plot of the velocity vectors in the (Tv)-plane. At these values of the Reynolds number a three-dimensional character has already developed but the flow structure in the (Lv)-plane is qualitatively similar to that obtained using the two-dimensional model. Figure 16 compares the horizontal velocity profiles on the surface (at the intersection of the free surface and the Lv-plane) obtained with the two-dimensional and the three-dimensional solutions at various values of Re, namely 2×10^3, 3×10^3 and 5×10^3. From this figure it is clear that the surface velocity profiles of the three-dimensional flow have the usual features of thermocapillary-driven flows in rectangular cavities and values comparable with the two-dimensional case except in the region near the cold wall. Note that in two-dimensional calculations, at $Re = 5 \times 10^3$, the curve exhibits two maxima which indicates that a two-cell configuration would already be present. However, the curve arising from the three-dimensional solution shows only one maximum and thus the overall structure of the flow must be different. Three-dimensional effects are relatively small at the top surface, but in the immediate vicinity of the endwalls the flow field displays strong three-dimensional behaviour with recirculations in the return flow in the lower part of the cavity. Another interesting feature shown in figure 15 is the fact that, for large Re, the surface velocity does not reach a maximum on the axis of symmetry (Lv-plane) but rather away from it. This feature may be related to

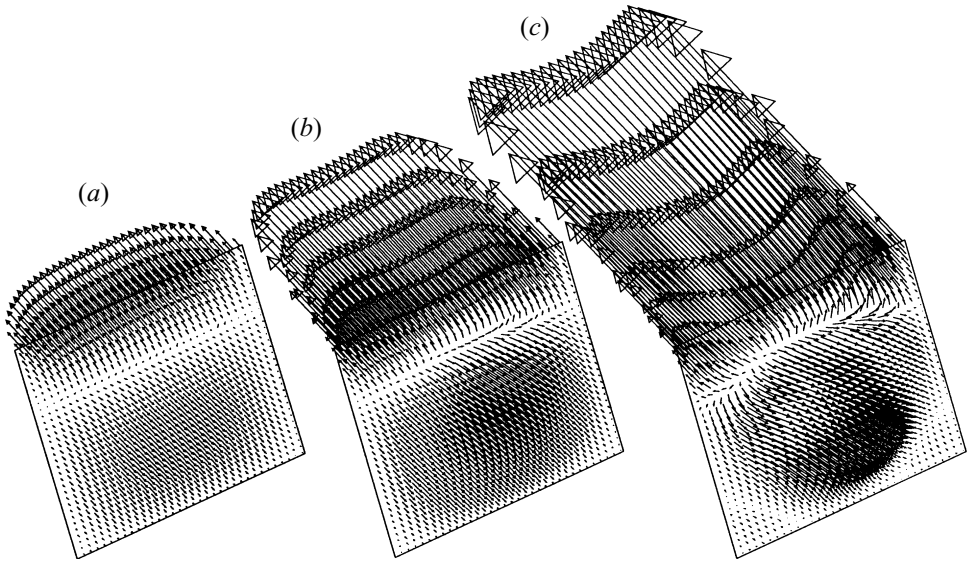

FIGURE 15. Thermocapillary steady flow solutions without a magnetic field ($Ha = 0$). The velocity vectors are plotted in the (Tv)-plane for three Reynolds numbers: (*a*) $Re = 5 \times 10^2$; (*b*) $Re = 2 \times 10^3$ and (*c*) $Re = 5 \times 10^3$.

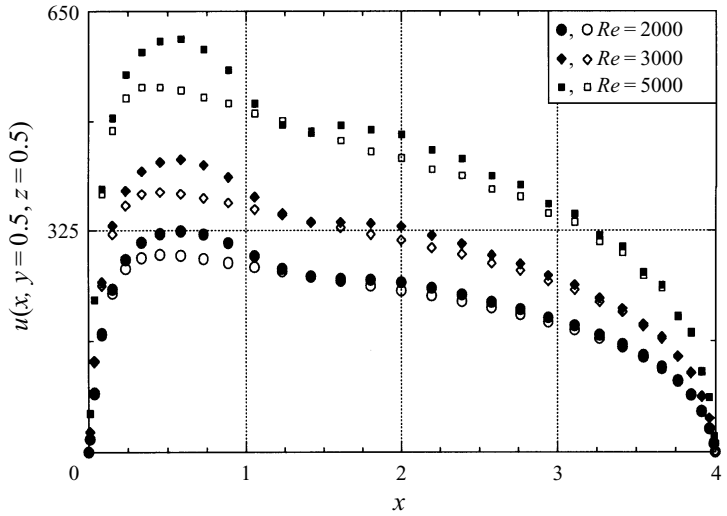

FIGURE 16. Comparison of the horizontal surface velocity profiles along the x-direction as a function of the Reynolds number ($Re = 2 \times 10^3$, 3×10^3 and 5×10^3) without a magnetic field ($Ha = 0$). The results are given for the two-dimensional case (filled symbols) and for the three-dimensional case in the (Lv)-plane (open symbols).

the structure of the flow in the lower part of the cavity. In fact, the flow is driven by a constant surface tension force on the whole upper surface. But, as the return longitudinal flow in the lower part of the cavity is rather concentrated in the core, this will give stronger vertical shear gradients and so a greater reduction of the velocity in the centre.

In the following, we present the results of a series of three-dimensional simulations

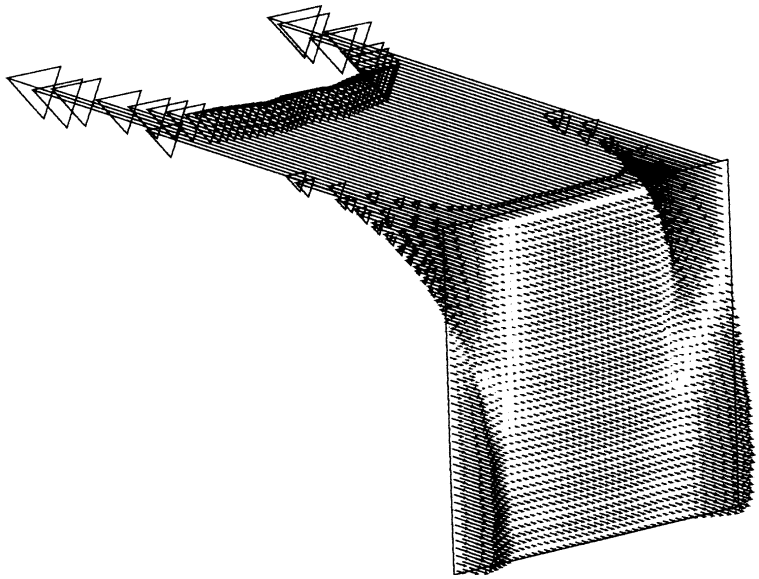

FIGURE 17. Velocity vectors in the (Tv)-plane for the thermocapillary flow and the B_z case at $Re = 2 \times 10^3$ and $Ha = 140$.

for the B_z case. The main features of the results are that, when the value of Ha is increased, the overall fluid circulation becomes less intense with progressive modification of the structure of the melt flow. In figure 17 the velocity vectors in the (Tv)-plane are displayed for $Ha = 140$. As shown in this figure, there is much more activity near the free surface, with overvelocity peaks along the lateral walls. This overvelocity is already apparent at $Ha = 20$. A further increase of Ha leads to additional changes in the flow structure. Owing to the progressive weakening of the cold-wall eddy as Ha is increased, the overall circulation pattern becomes increasingly invariant along x and antisymmetric with respect to the (Tv)-plane, and the centre of circulation moves towards the free surface. Furthermore, the viscous layer induced by the relatively large surface velocity, which is observed in the absence of a magnetic field, is also found, but has a much smaller thickness when Ha is increased. The structure of the vertical velocity in the (Lh)-plane bears a resemblance to that observed in the confined and free surface cases.

The electric potential in the (Tv)-plane is vertically still more asymmetric than in the free surface case, with stronger gradients in the upper part. In the central region (outside the parallel layers), a gradient of potential may be observed as in the free surface case, which could be responsible for an extra damping in the upper part compared to the two-dimensional case where only the directly induced electric current need be considered. But here, due to the strong velocities at the surface, this effect is not visible. The overall characteristics of the electric current density reflect those of the melt flow: in a given plane of constant x, one asymmetric current loop is found with much larger current density concentrated at the top, while the very weak returning current fills the remaining area. This current loop induces damping of the flow, but also creates overvelocities in the parallel layers.

We next consider results for the B_x case. The magnetic field has a weaker effect on the velocity than in the B_z case. Nonetheless, the plots of the velocity vectors in planes of constant x presented in figure 18 reveal effects of a magnetic field on the

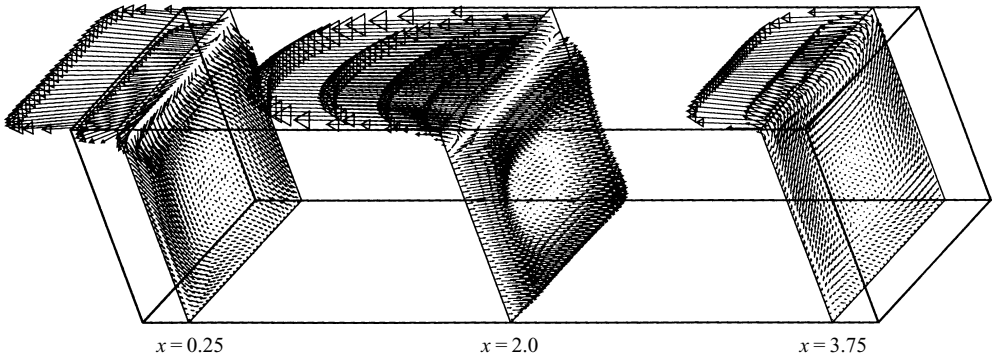

FIGURE 18. Velocity vectors in three planes of constant x for the thermocapillary flow and the B_x case at $Re = 2 \times 10^3$ and $Ha = 200$. The planes are located at $x = 0.25$, 2 and 3.75.

flow structure and predominantly three-dimensional behaviour. As in the B_z case one observes a large surface velocity, inducing a thin viscous layer, and a weak return flow which occupies a large part of the depth. But no overvelocities appear at the surface up to the largest value of Hartmann numbers, $Ha = 250$, we investigated. For large Ha (figure 18), a reverse circulation inside the returning flow becomes visible. This reverse circulation occurs despite the fact that no magnetic force acts in the longitudinal direction. In fact, here, due to the special structure of the flow, the directly induced electric current is mainly created by the vertical velocity and is strongest just below the upper surface. The electric potential is vertically asymmetric with stronger gradients in the upper part. The resulting electric current circulates mainly in planes of constant x and it consists of two superposed counter-rotating loops, a small one at the top and a large one in the core, which, as already described, generate longitudinal pressure gradients. In the upper part of the cavity the force resulting from the longitudinal pressure gradient reduces the action of the thermocapillary force while, in the lower part of the cavity, it induces the weak reverse flow already mentioned. Note that the size and the intensity of this zone of reversed flow is seen to increase as Ha increases. The behaviour of the vertical velocity in the (Lh)-plane as a function of Ha is found to be qualitatively similar to that observed for the free surface cavity in the B_x case.

From figure 18, it is also clear that the surface velocity is no longer monotonic in x. It displays a U-shaped transverse profile near the hot wall, and a parabolic (Poiseuille) transverse profile at mid-length in the cavity. Finally, near the vertical cold wall, it again takes on the U-shaped form. Note that this particular feature of the surface velocity, namely the appearance of a parabolic velocity profile, is not obtained in the case without a magnetic field when $Re = 2000$ but only at lower Reynolds numbers, e.g. $Re = 500$. In fact, this parabolic profile is only observable if the flow velocities are small enough that the distance for development which increases with Reynolds number, is smaller than the length of the cavity. Another interesting aspect of such flows is the fact that the intensity of the return flow increases with longitudinal distance. This aspect is made clearer by the plot of the horizontal velocity component profiles as a function of the z-coordinate at $y = 0.5$ and 0.85 and various x-locations in figure 19. This behaviour is consistent with the observed particle tracks (see figure 20) which show that as the flow progresses in the x-direction, secondary flows are fed by the surface layer to rejoin the overall returning flow; thus the velocity

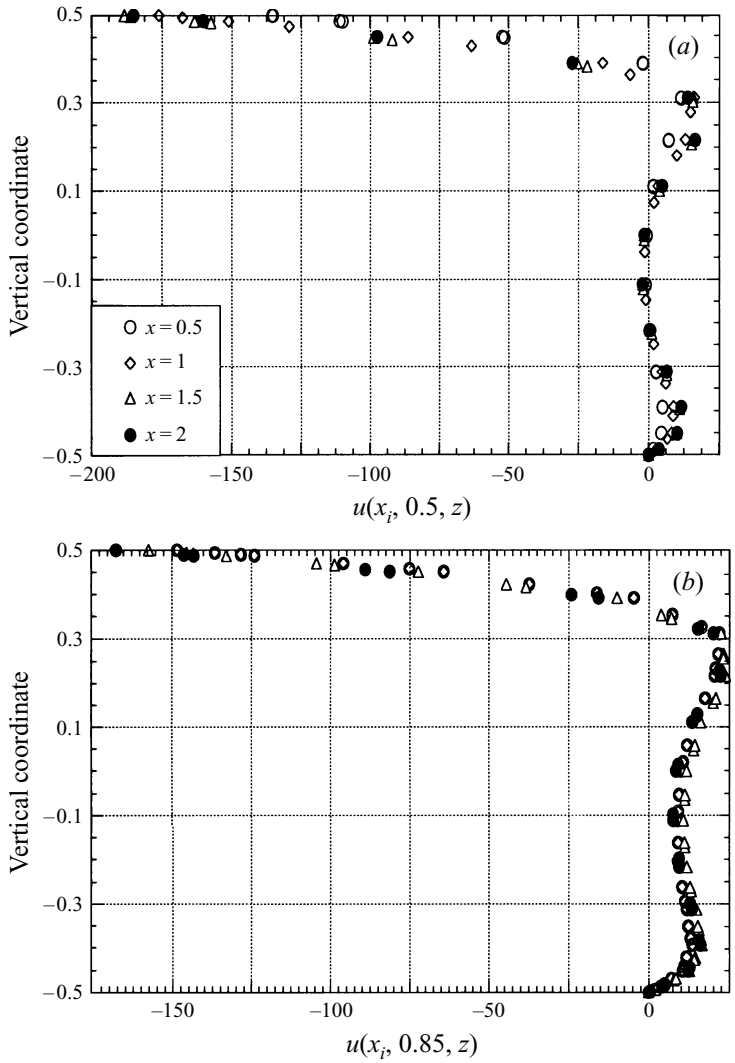

FIGURE 19. Thermocapillary steady flow solution for the B_x case at $Re = 2 \times 10^3$ and $Ha = 200$. The horizontal velocity profiles along z are given at various longitudinal locations ($x = 0.5$, 1, 1.5 and 2) and for two transversal locations: (*a*) $y = 0.5$ and (*b*) $y = 0.85$.

is progressively enhanced. However, at $Ha = 200$, in the vicinity of the (Lv)-plane we observe that the reverse flow becomes strong enough to modify the overall circulation and induces a new recirculation zone in the lower part of the cavity.

In order to assess the effects of the constant magnetic field upon the intensity of the flow, in figure 21 we plot the maxima of horizontal and vertical velocity as a function of Hartmann number. These curves exhibit changes in the response of the convective flow when $Ha > 10$ for the B_z case, while for the B_x case such changes occur when $Ha \geqslant 30$ and $Ha \geqslant 100$ for w_{max} and u_{max} respectively. From the figure we see that the behaviour of u_{max} and w_{max} depends on the orientation of the magnetic field. In fact, u_{max} varies as $Ha^{-1/2}$ and Ha^{-1} whereas w_{max} varies as $Ha^{-3/4}$ and $Ha^{-3/2}$, when the magnetic field is oriented along the positive x- and z-directions respectively.

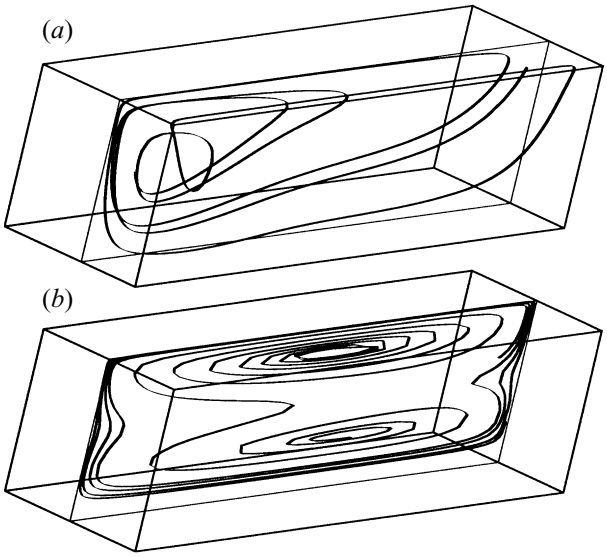

FIGURE 20. Plots of the particles tracks for the thermocapillary steady flow solutions and the B_x case for $Re = 2 \times 10^3$: (*a*) $Ha = 0$; (*b*) $Ha = 200$.

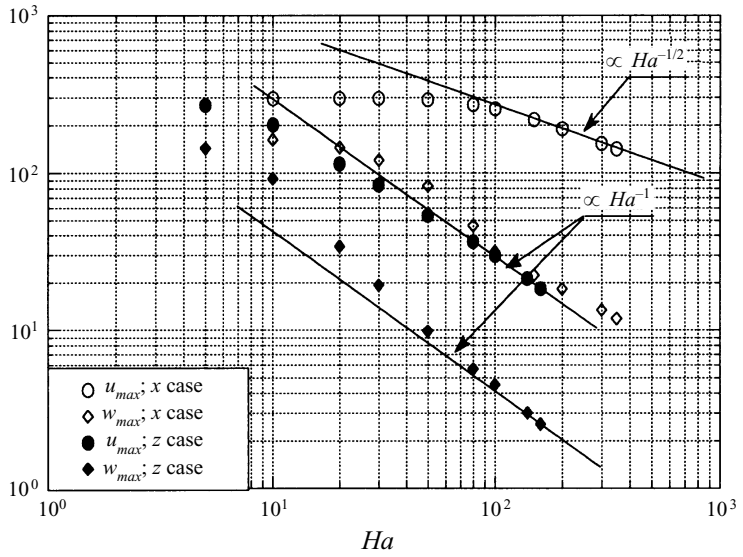

FIGURE 21. Plots of the maxima of the two main components of the velocity (u_{max} and w_{max}), for the thermocapillary flow case as a function of the Hartmann number for the B_z and the B_x cases.

5. Concluding remarks

This study of the effects of constant magnetic fields on flows of an electrically conducting melt has shown the occurrence of several important phenomena. One such finding is that increasing the strength of the magnetic field causes the solution to evolve progressively both in form and in magnitude: the absolute value of the velocity is markedly reduced and the overall distribution of the velocity is greatly modified. The numerical calculations further suggest that in the changing flow structure with increasing *Ha*, there are marked differences amongst the three configurations we

investigated, namely a confined cavity, a cavity with a zero-stress boundary on the top, and a cavity subjected to thermocapillary effects on the top.

Furthermore, the orientation of the applied magnetic field is found to have an important influence on the flow evolution. When the magnetic field is applied vertically (the B_z case) the general behaviour of the melt motion may be summarized as follows: for relatively small Ha, magnetic effects are primarily associated with braking of the average flow in the melt and, for sufficiently large Ha, the flow becomes unidirectional over a large part of the cavity with a quiescent core region surrounded at the bottom (and also at the top for the confined cavity) by Hartmann boundary layers and by parallel layers at the vertical sidewalls. In these parallel layers, peaks of overvelocity are observed which mainly concern the longitudinal velocity but also affect the vertical velocity. The boundary layer regime is attained for $Ha \geqslant 10$, a value independent of the boundary condition at the top. In the free surface case, strong effects of magnetic damping result in the inversion of the flow in the upper part of the cavity.

When the magnetic field is applied in the longitudinal direction (the B_x case) we also observe a decrease in the flow velocity with the creation of Hartmann and parallel layers, but these effects are established for larger Hartmann values, $Ha \geqslant 50$. In contrast with the B_z case, the Hartmann layers develop along the endwalls and the effect of overvelocity in the parallel layers mainly concerns the vertical velocity component. The vertical velocity is also non-zero throughout the cavity resulting in continuous transfer between the longitudinal upper and lower flows and preventing the establishment of a unidirectional flow. In addition, when Ha becomes large enough ($Ha > 200$), reverse flows become clearly visible in the core region of the cavity. In the thermocapillary-driven flow case, the appearance of this reverse flow leads to the splitting of the unicellular flow into two superposed cells.

The results of the analyses of the electric current effects, in both the B_x and B_z cases, are qualitatively similar and they show that at large values of Ha the behaviour of the flow is governed by the electric current distribution. This electric current has two components: the potential one, and the directly induced one which is principally responsible for the braking observed in the core region (it is the only contribution in the two-dimensional models). The electric potential maintains closed current lines, leading to a reduction of the damping in the parallel layers where the resulting current is almost parallel to the applied magnetic field. More subtle effects of current can give flow inversions in the core zones: in the B_z case, these inversions result from extra damping due to potential effects (similar to the electromagnetic pumping effect) with strong potential gradients in the parallel layers on either side of the core zone; in the B_x case, they correspond to pressure effects due to current loops perpendicular to the applied magnetic field. Furthermore, independently of the orientation of the applied magnetic field, the strongest electric current circulation occurs in the planes of constant x. This behaviour was to be expected in the B_z case. In the B_x case, it seems that enforcement of closure of current lines by potential effects occurs principally in transverse planes rather than in longitudinal planes because, owing to the smaller transverse cavity dimension, transverse potential gradients are stronger than longitudinal ones.

Comparison of the maxima of the velocity indicates that the magnetic damping is more efficient in the B_z case. This could be due to the fact that, in this case, the magnetic force $\boldsymbol{v} \times \boldsymbol{B} \times \boldsymbol{B}$ acts over larger areas and applies to the longitudinal velocity component, which is dominant.

Some aspects of our results in the B_z case, such as the presence of overvelocities in the parallel layers, have already been observed using the unidirectional flow hypothesis

(valid for $Ha \gg 1$) in two-dimensional simulations in transverse planes (Moreau & Ben Salah 1993, personal communication; Bojarevics 1995). Here, we have only discussed flows in cavities whose walls are perfect electric insulators. The opposite limit in which the walls are perfect electric conductors has also been investigated by Moreau & Ben Salah (1993, personal communication) and their findings show a stronger damping effect of the magnetic field.

We wish to thank Professor R. Moreau and Dr T. Alboussière from MADYLAM and Dr J. P. Garandet from CEN Grenoble for helpful discussions of this work. The authors acknowledge the valuable comments of Professor J. Scott (LMFA of Ecole Centrale de Lyon). This work was supported by the "Centre National des Etudes Spatiales" (Division Microgravité Fondamentale et Appliquée). Computations were carried out on a Cray YMP C98 computer, with the support from the CNRS through the "Institut du Développement et des Ressources en Informatique Scientifique".

REFERENCES

Afrid, M. & Zebib, A. 1990 Oscillatory three-dimensional convection in rectangular cavities and enclosures. *Phys. Fluids* A **2**, 1318–1327.

Alboussière, T., Garandet, J. P. & Moreau, R. 1993 Buoyancy-driven convection with a uniform magnetic field. Part 1. Asymptotic analysis. *J. Fluid Mech.* **253**, 545–563.

Baumgartl, J., Hubert, A. & Müller, G. 1993 The use of magnetohydrodynamic effects to investigate fluid flow in electrically conducting melts. *Phys. Fluids* A **5**, 3280–3289.

Baumgartl, J. & Müller, G. 1992 Calculation of the effects of magnetic field damping on fluid flow- Comparison of magnetohydrodynamic models of different complexity. In *Proc. VIIIth European Symp. on Materials and Fluid Sciences in Microgravity* (ESA SP-333), pp. 161–164. ESA Publ. Division c/o ESTEC, Noordwijk, The Netherlands.

Ben Hadid, H., Henry, D. & Kaddeche, S. 1997 Numerical study of convection in the horizontal Bridgman configuration under the action of a constant magnetic field. Part 1. Two-dimensional flow. *J. Fluid Mech.* **333**, 23–56.

Ben Hadid, H. & Roux, B. 1990*a* Thermocapillary convection in long horizontal layers of low-Prandtl-number melts subject to a horizontal temperature gradient. *J. Fluid Mech.* **221**, 77–103.

Ben Hadid, H. & Roux, B. 1990*b* Buoyancy-driven oscillatory flows in shallow cavities filled with low-Prandtl number fluids. In *Numerical Simulation of Oscillatory Convection in low-Pr Fluids* (ed. B. Roux). Notes on Numerical Fluid Mechanics, vol. 27, pp. 25–34. Vieweg.

Ben Hadid, H. & Roux, B. 1992 Buoyancy- and thermocapillary-driven flows in differentially heated cavities for low-Prandtl-number fluids. *J. Fluid Mech.* **235**, 1–36.

Bojarevics, V. 1995 Horizontal temperature gradient driven flow and its stability in a horizontal channel of rectangular cross-section with the effects of transversal magnetic field. In *Advances in Engineering Heat Transfer, Proc. Second Baltic Heat Transfer Conf.* (ed. B. Sunden, E. Blums & A. Zukauskas). Computational Mechanics Publications, Southampton Boston.

Carrière, P. & Jeandel, D. 1991 A 3D finite element method for the simulation of thermoconvective flows and its performances on a vector-parallel computer. *Intl J. Numer. Meth. Fluids* **12**, 929–946.

Carruthers, J. R. 1977 Thermal convection instabilities relevant to crystal growth from liquids. In *Preparation and Properties of Solid state Materials* (ed. W. R. Wilcox & R. A. Lefever), Vol. 3. M. Dekker.

Dupont, S., Marchal, J. M., Crochet, M. J. & Geyling, F. T. 1987 Numerical simulation of the horizontal Bridgman growth. Part 2. Three-dimensional flow. *Intl J. Numer. Meth. Fluids* **7**, 49–67.

Gill, A. E. 1974 A theory of thermal oscillations in liquid metals. *J. Fluid Mech.* **64**, 577–588.

Hart, J. E. 1972 Stability of thin non-rotating Hadley circulations. *J. Atmos. Sci.* **29**, 687–697.

Hart, J. E. 1983 A note on the stability of low-Prandtl-number Hadley circulations. *J. Fluid Mech.* **132**, 271–281.

HUNG, M. C. & ANDERECK, C. D. 1988 Transitions in convection driven by a horizontal temperature gradient. *Phys. Lett.* A **132**, 253–258.

HUNG, M. C. & ANDERECK, C. D. 1990 Subharmonic transitions in convection in a moderately shallow cavity. In *Numerical Simulation of Oscillatory Convection in low-Pr Fluids* (ed. B. Roux). Notes on Numerical Fluid Mechanics, vol. 27, pp. 338–343. Vieweg.

HURLE, D. T. J., JAKEMAN, E. & JOHNSON, C. P. 1974 Convective temperature oscillations in molten gallium. *J. Fluid Mech.* **64**, 565–576.

KADDECHE, S., BEN HADID, H. & HENRY, D. 1994 Macrosegregation and convection in the horizontal Bridgman configuration. I. Dilute alloys. *J. Cryst. Growth* **135**, 341–353.

KARNIADAKIS, G. E., ISRAELI, M. & ORSZAG, S. A. 1991 High-order splitting method for the incompressible Navier-Stokes equations. *J. Comput. Phys.* **97**, 414–443.

KIM, D. H., ADORNATO, P. M. & BROWN, R. A. 1988 Effect of vertical magnetic field on convection and segregation in vertical Bridgman crystal growth. *J. Cryst. Growth* **89**, 339–356.

KUHL, R. & WILKE, H. 1990 Buoyant convection of low Prandtl number melts in horizontal boat configuration. In *41st Congress of the International Astronautical Federation, October 6-12, Dresden, GDR* (IAF-90-398).

KUO, H. P. & KORPELA, S. A. 1988 Stability and finite amplitude natural convection in a shallow cavity with insulated top and bottom and heated from a side. *Phys. Fluids* **31**, 33–42.

LAURE, P. & ROUX, B. 1987 Synthèse des résultats obtenus par l'étude de stabilité des mouvements de convection dans une cavité horizontale de grande extension. *C. R. Acad. Sci. Paris* **305**, 1137–1143.

MOTAKEF, S. 1990 Magnetic field elimination of convective interference with segregation during vertical-Bridgman growth of doped semiconductors. *J. Cryst. Growth* **104**, 833–850.

MÜLLER, G. 1993 Convective instabilities in melt growth configurations. *J. Cryst. Growth* **128**, 26–36.

MUNDRANE, M. & ZEBIB, A. 1993 Two- and three-dimensional buoyant thermocapillary convection. *Phys. Fluids* A **5**, 810–818.

OREPER, G. M. & SZEKELY, J. 1983 The effect of an externally imposed magnetic field on buoyancy driven flow in a rectangular cavity. *J. Cryst. Growth* **64**, 505–515.

OREPER, G. M. & SZEKELY, J. 1984 The effect of a magnetic field on transport phenomena in a Bridgman-Stockbarger crystal growth. *J. Cryst. Growth* **67**, 405–419.

OZOE, H. & OKADA, K. 1989 The effect of the direction of the external magnetic field on the three-dimensional natural convection in a cubical enclosure. *Intl J. Heat Mass Transfer* **32**, 1939–1954.

PATERA, A. J. 1984 A spectral element method for fluid dynamics : Laminar flow in a channel expansion. *J. Comput. Phys.* **54**, 468–488.

PRATTE, J. M. & HART, J. E. 1990 Endwall driven, low Prandtl number convection in a shallow rectangular cavity. *J. Cryst. Growth* **102**, 54–68.

ROUX, B. (ED.) 1990 *GAMM Workshop: Numerical Simulation of Oscillatory Convection in low-Pr Fluids.* Notes on Numerical Fluid Mechanics, vol. 27. Vieweg.

SERIES, R. W. & HURLE, D. T. J. 1991 The use of magnetic fields in semiconductor crystal growth. *J. Cryst. Growth* **113**, 305–328.

WANG, T. M., KORPELA, S. A., HUNG, M. C. & ANDERECK, C. D. 1990 Convection in a shallow cavity. In *Numerical Simulation of Oscillatory Convection in low-Pr Fluids* (ed. B. Roux). Notes on Numerical Fluid Mechanics, vol. 27, pp. 344–353. Vieweg.